J. Fluid Mech. (2021), *vol*. 928, A28, doi:10.1017/jfm.2021.844

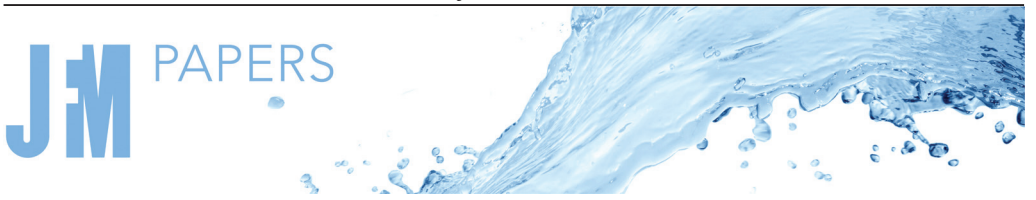

A model to predict the oscillation frequency for drops pinned on a vertical planar surface

J. Sakakeeny[1], C. Deshpande[2], S. Deb[2], J.L. Alvarado[2,3] and Y. Ling[1,†]

[1]Department of Mechanical Engineering, Baylor University, Waco, TX 76643, USA

[2]Department of Mechanical Engineering, Texas A&M University, College Station, TX 77843, USA

[3]Department of Engineering Technology and Industrial Distribution, Texas A&M University, College Station, TX 77843, USA

(Received 1 June 2021; revised 6 August 2021; accepted 21 September 2021)

Accurate prediction of the natural frequency for the lateral oscillation of a liquid drop pinned on a vertical planar surface is important to many drop applications. The natural oscillation frequency, normalized by the capillary frequency, is mainly a function of the equilibrium contact angle and the Bond number (*Bo*), when the contact lines remain pinned. Parametric numerical and experimental studies have been performed to establish a comprehensive understanding of the oscillation dynamics. An inviscid model has been developed to predict the oscillation frequency for wide ranges of *Bo* and the contact angle. The model reveals the scaling relation between the normalized frequency and *Bo*, which is validated by the numerical simulation results. For a given equilibrium contact angle, the lateral oscillation frequency decreases with *Bo*, implying that resonance frequencies will be magnified if the drop oscillations occur in a reduced gravity environment.

Key words: contact lines, drops

1. Introduction

Effective drop removal from a condenser surface is critical to highly efficient dropwise condensation, which is in turn important to many applications such as condensation heat transfer (Yao *et al.* 2017) and water harvesting (Dai *et al.* 2018). The recent advancement on superhydrophobic surfaces (Boreyko & Chen 2009*b*; Yao *et al.* 2017) have shown promising enhancement of droplet mobility. Nevertheless, high mobility of drops on superhydrophobic surfaces can be lost when the condensate nucleates within the texture and the wetting falls into the Wenzel state. To restore the high drop mobility, external forcing such as surface vibration is typically required to excite the oscillation of the drops and to revert the wetting to the Cassie state (Boreyko & Chen 2009*a*; Yao *et al.* 2017).

† Email address for correspondence: stanley_ling@baylor.edu

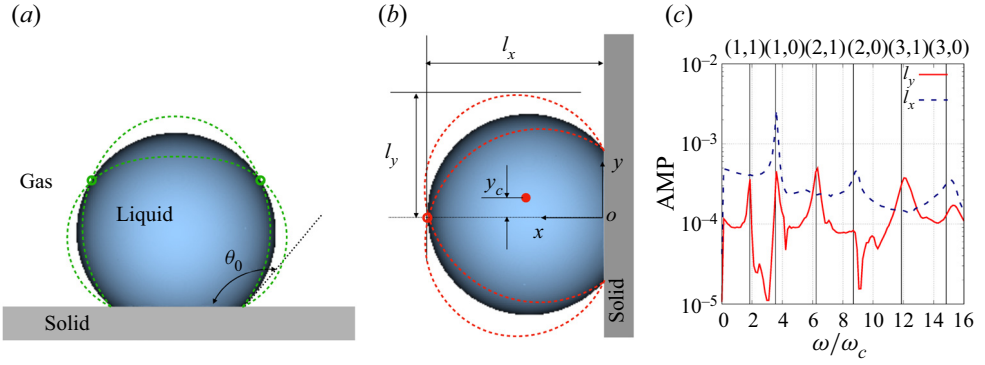

Figure 1. Schematics of the (*a*) longitudinal ($n = 1$, $m = 0$) and (*b*) lateral ($n = 1$, $m = 1$) oscillation modes for a drop on a flat surface with pinned contact lines. The red and green open circles indicate the longitudinal and azimuthal nodal lines, while the red filled circle indicates the centroid of the deformed drop. (*c*) Simulation results for the frequency spectra for the maximum interfacial locations l_x and l_y, for $\theta_0 = 100^\circ$ and $Bo = 0$. The Bostwick & Steen (2014) model predictions for modes (n, m) are shown (see vertical lines) for comparison.

When the excitation frequency matches the natural frequency, the oscillation amplitude of the drop is maximized for a given energy input due to the resonance effect (Noblin, Buguin & Brochard-Wyart 2004; Boreyko & Chen 2009*a*; Yao *et al.* 2017). Therefore, it is highly advantageous to predict the natural oscillation frequencies for drops on surfaces of different wettability.

Similar to a free drop, the oscillation of a drop supported by a planar surface can be characterized by spherical-harmonic modes, with n and m representing the longitudinal and azimuthal wavenumbers, respectively (Strani & Sabetta 1984; Bostwick & Steen 2014). Different from free drops, the two $n = 1$ modes, corresponding to the centroid translation in the directions normal ($n = 1, m = 0$) and tangential ($n = 1, m = 1$) to the surface, trigger shape oscillations for supported drops. Since the natural frequency and damping rate increase with n (Lamb 1932), the $n = 1$ modes typically dominate the oscillations of supported drops (Strani & Sabetta 1984; Noblin *et al.* 2004; Sakakeeny & Ling 2020, 2021). While the longitudinal mode ($n = 1, m = 0$) is axisymmetric, see figure 1(*a*), and has been extensively studied (Strani & Sabetta 1984, 1988; Noblin *et al.* 2004; Sakakeeny & Ling 2020, 2021), less attention has been paid to the lateral mode ($n = 1, m = 1$), see figure 1(*b*), which is the focus of the present study.

In the limit of zero gravity, different inviscid theoretical models (Strani & Sabetta 1984; Celestini & Kofman 2006; Bostwick & Steen 2014) have been developed to predict the frequency of different spherical-harmonic modes, including the lateral mode of interest here. As the effect of gravity is characterized by the Bond number (Bo), the aforementioned inviscid models are strictly valid only in the limit of zero Bo, although the model predictions were observed to agree reasonably well with experiment for drops with small Bo (Chang *et al.* 2015). A simple capillary–gravity wave model has been suggested by Noblin *et al.* (2004) to include the effect of gravity on the oscillation frequency, but significant discrepancies with experiment was found for surfaces with large contact angles (Yao *et al.* 2017). Numerical simulations have been recently performed by Sakakeeny & Ling (2020, 2021) to investigate the effect of Bond number on the axisymmetric zonal oscillation modes for supported drops. Their results indicated that the drop oscillation frequency varies significantly with Bo, even when the drop radius is smaller than the capillary length ($Bo < 1$). Furthermore, they also found that the orientation of the supporting surface, with respect to the gravitational acceleration, also

r	m	Oh	θ_0	Bo
ρ_g/ρ_l	μ_g/μ_l	$\mu_l/\sqrt{\rho_l\sigma R_d}$	(deg.)	$\rho_l g R_d^2/\sigma$
0.0012	0.01	0.00239	50–150	0–0.78

Table 1. Key parameters for simulations.

matters: while the drop oscillation frequency increases with Bo for sessile drops, the frequency decreases with Bo for pendant drops. To the knowledge of the authors, there are no former experimental or numerical studies in the literature that systematically address the effects of Bo and equilibrium contact angle on the oscillation of drops pinned on a vertical planar surface. In the present study, a combined numerical, experimental and theoretical analysis is performed for the lateral oscillation of a water drop on a vertical planar surface. The goal of the study is to establish a model to predict the oscillation frequency for a drop at small but finite Bo. We focus only on drops with pinned contact lines, since they are the ones that require oscillation excitation to restore high mobility.

2. Methods

2.1. *Key parameters*

The shape oscillation of a liquid drop is mainly controlled by surface tension. The contact with the solid surface has a significant impact on the oscillation dynamics. The natural frequency of the drop oscillation depends on the equilibrium contact angle (θ_0), contact line mobility and Bo (Bostwick & Steen 2014; Sakakeeny & Ling 2020, 2021). The key dimensionless parameters and the ranges of values considered are summarized in table 1. Due to the small gas-to-liquid density and viscosity ratios, $r = \rho_g/\rho_l$ and $m = \mu_g/\mu_l$, the effect of the surrounding gas is generally small. The effects of gravity and liquid viscosity, compared with surface tension, are characterized by the Bond and Ohnesorge numbers, $Bo = \rho_l g R_d^2/\sigma$ and $Oh = \mu_l/\sqrt{\rho_l\sigma R_d}$, where g and σ are gravity and surface tension, while $R_d = (3V_d/4\pi)^{1/3}$ is the radius based on the drop volume V_d. For millimetre-size water drops, Oh and Bo are smaller than one. As a result, the oscillation frequency ω generally scales with the capillary frequency (Lamb 1932), $\omega_c = \sqrt{\sigma/(\rho_l R_0^3)}$, where R_0 is the radius of the equilibrium spherical-cap shape when gravity is absent, and $R_0 = R_d((2 + cos\theta_0)(1 - cos\theta_0)^2/4)^{-1/3}$. The reason for using R_0, instead of R_d is because R_0 better represents the radius of curvature.

While r, m and Oh are fixed in the simulation, the equilibrium contact angle θ_0 is varied from 50° to 150° to cover a wide range of wettability, varying from hydrophilic to superhydrophobic surfaces. For a given liquid, Bo can be varied by changing V_d or g. In the present study, we keep V_d fixed and vary g, yielding $0 \leq Bo \leq 0.78$. Except for very small Bo, the simulation results also well represent cases for drops with different V_d under full gravity. Although Bo is smaller than unity for all cases considered, namely R_0 is smaller than the capillary length $\sqrt{\sigma/(\rho_l g)}$, it will be shown later that the effect of gravity on the oscillation frequency can be significant.

2.2. *Simulation methods*

The numerical simulations were conducted using the *Basilisk* solver, in which the Navier–Stokes equations are solved by a finite-volume approach. The sharp interface

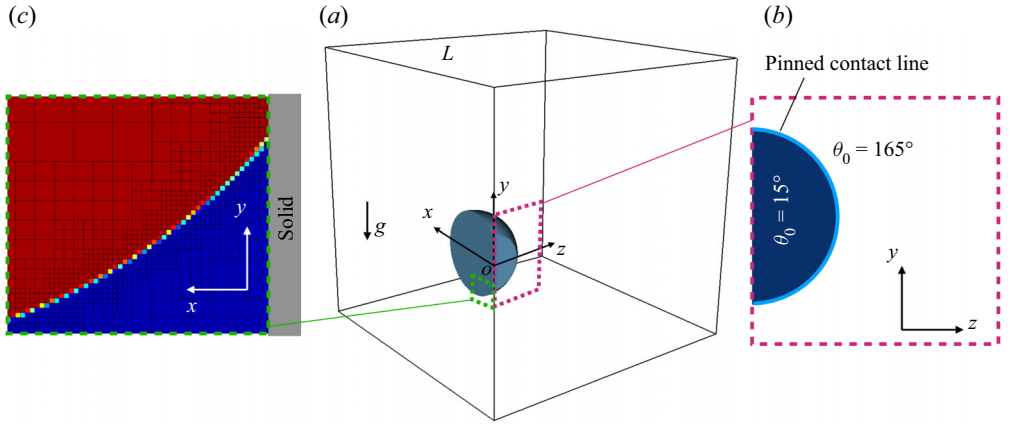

Figure 2. (*a*) The simulation domain. (*b*) Close up of the field of liquid volume fraction f on the contact plane ($x = 0$), showing the pinned contact line circle and the small and large θ_0 specified inside and outside of the contact line. (*c*) Close up of the symmetric plane ($z = 0$), showing the adaptive mesh and VOF field.

is captured by the volume-of-fluid (VOF) method (Scardovelli & Zaleski 1999). The balanced-force method is used to discretize the surface tension (Popinet 2009). The height-function method is used to calculate the interface curvature (Popinet 2009) and to specify the contact angle at the surface (Afkhami & Bussmann 2009). Details of the numerical methods and validation studies for the *Basilisk* solver can be found in previous studies (Sakakeeny & Ling 2020, 2021) and the code website.

The computational domain is a cube with the edge length $L = 8R_d$, see figure 2(*a*). The drop is symmetric with respect to the plane $z = 0$ for the lateral mode, so only half of the drop is simulated. The surface $x = 0$ is in contact with the drop and is taken as a no-slip wall. Other boundaries are slip walls. Although modelling of mobile contact lines is challenging (Snoeijer & Andreotti 2013; Afkhami *et al.* 2018), here, we consider only the asymptotic limit such that the contact lines are pinned. Physically, this limit occurs when the hysteresis effect is very strong and the oscillation amplitude is small. The pinning of contact lines is achieved by imposing very small and large contact angles, i.e. $\theta_0 = 15°$ and $165°$, inside and outside of the contact line on the surface $x = 0$, see figure 2(*b*), to mimic the strong hysteresis effect. As long as the contact angle θ remains bounded by these two values when the drop oscillates, the contact line cannot recede or advance. Validation of this treatment of the contact lines can be found in our previous study (Sakakeeny & Ling 2021). The drop oscillations are initiated by specifying an initial shape different from the equilibrium shape or by increasing the gravity for a short period. The oscillation frequency will not be affected if the amplitudes of excited oscillations are small.

An adaptive octree mesh is used for spatial discretization, see figure 2(*c*), and the maximum refinement level is $\mathcal{L} = 10$, corresponding to $R_d/\Delta_{min} = 128$, where Δ_{min} is the minimum cell size. The adaptation thresholds for the liquid volume fraction (f) and the fluid velocity components (u, v, w) are 0.0001 and 0.01, respectively. It is verified that the refinement level and error thresholds are sufficient to yield mesh-independent results. The simulations were performed on the cluster *Kodiak* using 144 CPU cores (Intel E5-2695 V4). Each simulation case takes approximately 15 days to reach the time $t\omega_c \approx 110$. The simulation time has been verified to be sufficiently long for accurate measurement of frequencies from the spectra. To vary both θ_0 and Bo, there are in total approximately 30 cases simulated.

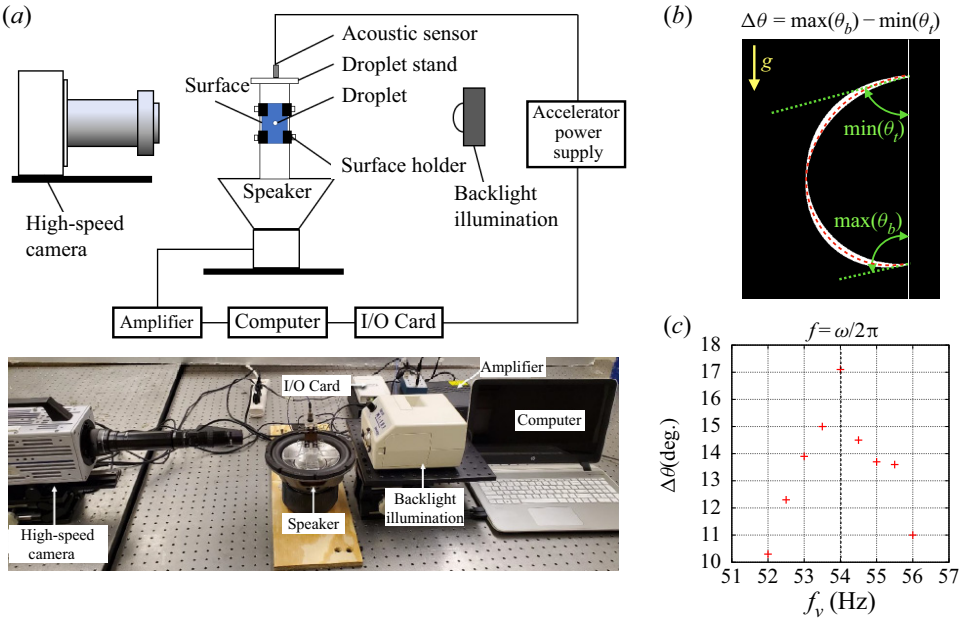

Figure 3. (*a*) Experimental set-up. (*b*) Superimposition of drop edges on the central plane from 100 snapshots for the polystyrene surface and drop volume 4.78 µl. The red dashed line indicates the equilibrium shape. The contact angles at the top and bottom of the drop, θ_t and θ_b, are measured. The maximum contact angle hysteresis is defined as $\Delta\theta = \max(\theta_b) - \min(\theta_t)$. (*c*) Variation of $\Delta\theta$ as a function of the surface vibration frequency f_v. The resonance angular frequency $\omega = 2\pi f$ is identified as the peak of the function.

Figure 1(*c*) shows the frequency spectra of the maximum interfacial locations in x and y directions, l_x and l_y, for $\theta_0 = 100^\circ$ and $Bo = 0$. The different oscillation modes are clearly identified: while the spectrum for l_y shows the $m = 1$ modes, that for l_x indicates the $m = 0$ modes. The frequencies predicted by the inviscid model of Bostwick & Steen (2014) (B–S) for (n, m) modes are shown for comparison, see the vertical lines. The simulation results generally agree very well with the inviscid model, although small discrepancies were observed for the high-order (3, 0) and (3, 1) modes. It can be seen that the lateral mode considered in the present study exhibits the lowest frequency.

2.3. *Experimental methods*

Experiments have also been performed to measure the oscillation frequency of the lateral mode. The drop oscillations were excited by the lateral vibration of the supported substrate. Distilled water drops were placed on the vertical substrate, which was fixed to a drop stand, see figure 3(*a*). The stand was attached to a sound speaker (Infinity Reference 860 W, Infinity Inc.) with an amplifier system (Russound P75-2 Channel Dual Source 75 W). The speaker provided sine wave vibrations of different frequencies to the substrate using a connected online tone generator. An accelerometer (352C04, PCB Piezoelectronics) was used to measure vibration frequencies and acceleration of the substrate. A National Instruments Data Acquisition System (NI USB-5132) was used to interface the accelerometer with the computer. A high-speed camera (Photron SA3) with a halogen lamp (Fiber-Lite MI series, Dolan-Jenner Inc.) was used to capture the drop deformation.

Substrate	θ_0 (deg.)	V_d (μl)
Al 6061	74.2 ± 1.80	3.30, 3.79, 4.29, 4.78
Cu 110	85.5 ± 1.30	3.30, 3.79, 4.29, 4.78
Polystyrene	93.0 ± 1.06	3.30, 3.79, 4.29, 4.78
PTFE	100.6 ± 0.70	3.30, 3.79, 4.29, 4.78
Wax	105.0 ± 0.60	3.30, 3.79, 4.29, 4.78

Table 2. Experimental cases. PTFE, polytetrafluoroethylene.

The different substrates and drop volumes tested are summarized in table 2. Five different commercially available substrates with increasing θ_0 were used. For each substrate, four different droplet volumes were tested. The wax substrate was prepared in house by firmly attaching wax paper on the polystyrene surface. All substrates, except for the wax one, were cleaned with isopropyl alcohol, distilled water and air dried before testing. The ranges of parameters considered in the simulation are wide enough to cover all the experimental cases.

For a given acceleration of the substrate, the excited drop oscillation amplitude is maximized when the substrate vibration frequency ω_v matches the natural frequency ω. The acceleration amplitude is controlled to be small to avoid drop sliding on the surface. Different ω_v were imposed, and the range of ω_v tested was estimated based on the theoretical model of Celestini & Kofman (2006) (C–K). For each ω_v, 100 drop images were recorded. The drop contours on the central plane were identified using the Canny method in MATLAB and superimposed as shown in figure 3(*b*). The contact angles at the top and bottom of the drops θ_t and θ_b are measured. The maximum contact angle difference, $\Delta\theta = \max(\theta_b) - \min(\theta_t)$, is used to characterize the excited drop oscillation amplitude. The resonance frequency $\omega = 2\pi f$ is then identified by the local maximum of $\Delta\theta$ as a function of $\omega_v = 2\pi f_v$, see figure 3(*c*). A small f_v increment of 0.5 Hz were used near the local maximum for accurate measurement.

3. Results and discussion

3.1. *Oscillation frequency*

The simulation and experimental results for the oscillation frequency of the lateral mode ω are shown in figure 4. The results of previous experiments by C–K and Sharp, Farmer & Kelly (2011), and theoretical models by C–K and B–S are also included for comparison. It is observed that the experimental data for different drop volumes collapse approximately, when ω is normalized by ω_c. This scaling relation $\omega \sim \omega_c$ indicates $\omega \sim V_d^{3/2}$, which is consistent with previous observations for a minor gravity effect (Noblin *et al.* 2004). The normalized frequency ω/ω_c for different V_d still varies slightly due to the effect of Bo. For the experiments of C–K ($0.04 \lesssim Bo \lesssim 0.19$) and Sharp ($0.16 \lesssim Bo \lesssim 0.66$), the surface is horizontal, ω/ω_c increases with Bo (Sakakeeny & Ling 2021), while for the present experiment ($0.12 \lesssim Bo \lesssim 0.16$) that uses vertical surfaces, ω/ω_c decreases with Bo (as shown later in figure 7). When Bo decreases, the experimental results for different surface orientations approach to the simulation results for $Bo = 0$.

The B–S model assumes $Bo = 0$, so the equilibrium drop is a spherical cap. The inviscid linear stability theory is used to predict the frequency of the oscillation. The B–S predictions generally agree well with simulation results, see figure 4. Small discrepancies

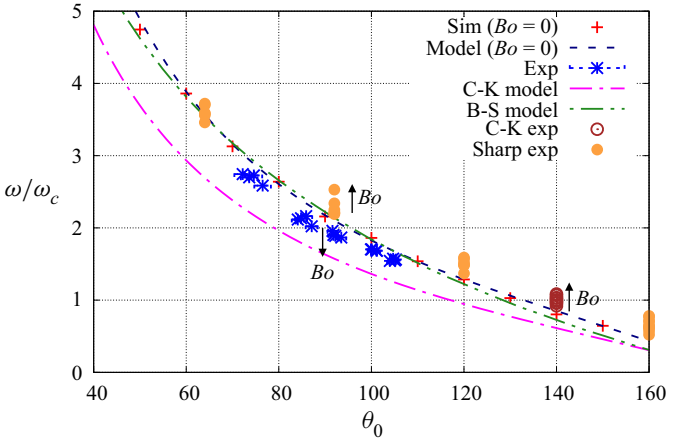

Figure 4. Present simulation, model and experimental results for the frequency of the lateral oscillation mode as a function of the equilibrium contact angle θ_0 for $Bo = 0$, compared with previous models and experiments by C–K, Sharp *et al.* (2011) and B–S. The experiments of C–K and Sharp are for sessile drops on a horizontal surface, for which the normalized frequency increases with Bo, while the present experiments are for a vertical surface, where the frequency decreases with Bo. The arrows indicate the variation of the normalized frequency as Bo increases. When Bo decreases, the experimental results for different surface orientations approach the simulation and model results for $Bo = 0$.

are observed for $\theta_0 \gg 90°$, which may be due to the simplified contact line boundary conditions used in the B–S model (Sakakeeny & Ling 2020). The C–K model predicts the frequency by a different approach. The shape oscillation of the drop is modelled as a harmonic oscillator, so the frequency is $\omega = \sqrt{k/m_d}$, where m_d is the drop mass. The effective spring constant k is related to surface tension, which serves as a restoring force to bring the drop back to its equilibrium state. The C–K model is more convenient to use since an explicit expression of ω is given, but it significantly under-predicts the frequencies, as shown in figure 4 and also in the original paper of C–K.

3.2. *An inviscid model to predict oscillation frequency*

A new inviscid model is developed in this study. The goal is to achieve an explicit expression to accurately predict the oscillation frequency. Furthermore, the new model incorporates the effect of finite Bo, which is ignored in B–S and C–K models. We take the equilibrium state for $Bo = 0$ as the reference state, where the y-coordinate of the centroid and the drop surface area are $y_c = y_{c0} = 0$ and $S = S_0$, respectively. The surface energy of the drop is $E_s = \sigma(S - S_0)$. The surface area $S - S_0$ can be expanded as a function of $y_c - y_{c0}$

$$\frac{S - S_0}{S_0} = \eta \left(\frac{y_c - y_{c0}}{R_0} \right)^2 + \xi \left(\frac{y_c - y_{c0}}{R_0} \right)^4. \tag{3.1}$$

Due to symmetry, only the even-order terms remain and the terms higher than fourth order are truncated, assuming small oscillation amplitudes. The relation between S and y_c during oscillation is assumed to be similar to that for a static equilibrium drop under different body forces (Celestini & Kofman 2006). As a result, the parameters η and ξ depend only on θ_0 and can be obtained from the solution for static drops. The *Surface Evolver* code was used to obtain the static solutions for different body forces for a given θ_0, which are then used to measure η and ξ following (3.1). The procedures are similar to our previous

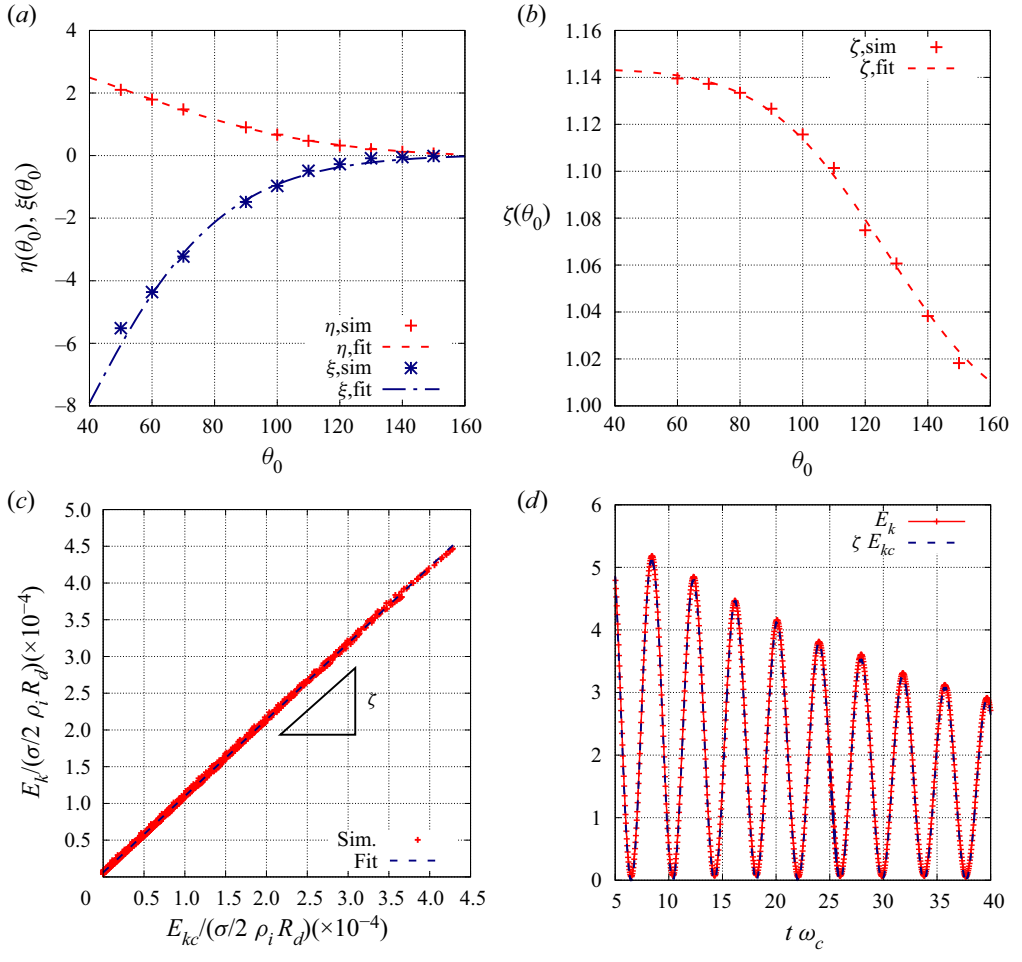

Figure 5. Model parameters (*a*) η and ξ and (*b*) ζ as functions of θ_0; (*c*) E_k as a function of E_{kc} and (*d*) temporal evolution of E_k and the approximation ζE_{kc} for $\theta_0 = 140^\circ$ and $Bo = 0$.

study (Sakakeeny & Ling 2020) and thus are not repeated here. The results for η and ξ are shown in figure 5(*a*). For convenient use of the results, fitted correlations are provided

$$\eta(\theta_0) = a_0 \left[\exp\left(a_1(\cos\theta_0 + 1)\right) - 1\right], \tag{3.2}$$

$$-\xi(\theta_0) = b_0 \left[\exp\left(b_1(\cos\theta_0 + 1)\right) - 1\right], \tag{3.3}$$

where the fitting coefficients $[a_0, a_1] = [0.52.0.99]$ and $[b_0, b_1] = [0.20, 2.11]$. In the asymptotic limit $\theta_0 \to 180^\circ$, both η and ξ approach zero, since in that limit the lateral mode does not induce deformation. The static solutions also indicate that $\eta > 0$ and $\xi < 0$ for all θ_0.

The gravitational potential energy is expressed as $E_g = m_d g(y_c - y_{c0})$, and the overall potential energy is $E_p = E_s + E_g$. The equilibrium state is located at the minimum of E_p, namely $\mathrm{d}E_p/\mathrm{d}y_c = 0$, which yields

$$2\eta(y_{c1}/R_0) + 4\xi(y_{c1}/R_0)^3 + Bo_1 = 0, \tag{3.4}$$

where $Bo_1 = mgR_0/\sigma S_0 = 0.42(2+\cos\theta_0)^{1/3}(1-\cos\theta_0)^{-1/3}Bo$. The cubic equation can be solved for the equilibrium centroid position y_{c1}, near which E_p can be expanded as

$$E_p = \frac{1}{2}\frac{\mathrm{d}^2E_p}{\mathrm{d}y_c^2}(y_c - y_{c1})^2 = \sigma S_0 \eta_1 \left(\frac{y_c - y_{c1}}{R_0}\right)^2, \tag{3.5}$$

where $\eta_1 = \eta + 6\xi(y_{c1}/R_0)^2$. Although the exact solution exists for (3.4), we use the approximation $y_{c1} \approx -Bo_1/2\eta$ by neglecting the cubic term. Then we get the approximation

$$\eta_1 \approx \eta + \frac{3\xi}{2\eta^2}Bo_1^2. \tag{3.6}$$

The kinetic energy of the drop fluid is $E_k = \rho_l \int_{V_d} |\boldsymbol{u}|^2/2\,\mathrm{d}V$, which is evaluated in the simulation by the integral over the domain $E_k = \rho_l \int f(u^2+v^2+w^2)\,\mathrm{d}V$, where f is the liquid volume fraction, and u, v and w are the velocity components. If the drop moves as a rigid body, the kinetic energy would be $E_{kc} = m_d v_c^2/2$, where $v_c = \mathrm{d}y_c/\mathrm{d}t$ is the y-component of the centroid velocity. Due to the internal flow with respect to the centroid induced by the shape oscillation, $E_k > E_{kc}$ (Sakakeeny & Ling 2021). Furthermore, as shown in figure 5(*c*), E_k is approximately a linear function of E_{kc} when the drop oscillates. This is due to the fact that the temporal evolutions of energy of the internal flow and the magnitude of v_c are in phase. As a result, the kinetic energy correction factor, defined as $\zeta = E_k/E_{kc}$, is approximately a constant in time and can be measured from the simulation results as shown in figure 5(*c*). Then we can approximate

$$E_k \approx \zeta E_{kc} = \zeta m_d v_c^2/2. \tag{3.7}$$

The temporal evolutions of E_k and ζE_{kc} are plotted in figure 5(*b*) and the latter is affirmed to be generally a good approximation for all time. Further tests show that ζ varies little over Bo and is only a function of θ_0, see figure 5(*b*). The fitted function for ζ is given as

$$\zeta(\theta_0) = c_1 \mathrm{erf}\left[(\cos\theta_0 + 1)/c_2\right] + 1, \tag{3.8}$$

where the fitting coefficients $[c_1, c_2] = [0.14, 0.93]$. In the asymptotic limit $\theta_0 \to 180^\circ$, $\zeta \to 1$ since there is no shape oscillation and the lateral mode corresponds to rigid-body translation of the drop.

The total energy $E = E_p + E_k$ is constant in time, so $\mathrm{d}E/\mathrm{d}t = 0$. With (3.5) and (3.7) we obtain

$$k(y_c - y_{c1}) + m_d \frac{\mathrm{d}^2(y_c - y_{c1})}{\mathrm{d}t^2} = 0, \tag{3.9}$$

where $k = 2\sigma S_0 \eta_1/(\zeta R_0^2)$. The oscillation frequency $\omega = \sqrt{k/m_d}$ can be expressed as

$$\frac{\omega^2}{\omega_c^2} = \frac{12\left(\eta + \dfrac{3\xi}{2\eta^2}Bo_1^2\right)}{\zeta(2+\cos\theta_0)(1-\cos\theta_0)}. \tag{3.10}$$

In the limit of $Bo = 0$, (3.10) reduces to

$$\frac{\omega^2}{\omega_c^2} = \frac{12\eta}{\zeta(2+\cos\theta_0)(1-\cos\theta_0)}. \tag{3.11}$$

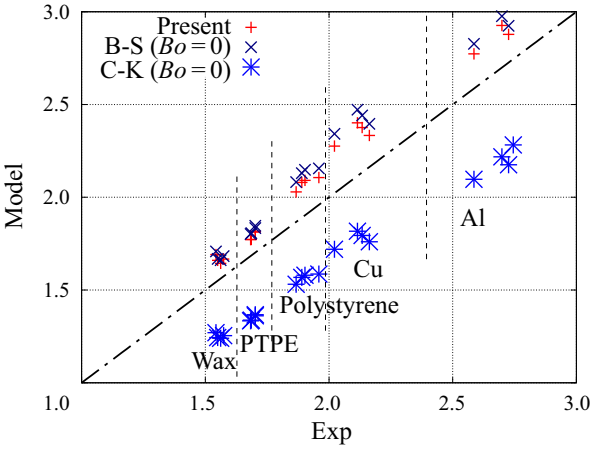

Figure 6. Comparison between experimental results of the normalized frequency ω/ω_c and model predictions with the present, B–S and C–K models.

The results of (3.11) are plotted in figure 4, which are shown to agree remarkably well with the simulation results. The C–K model for $Bo = 0$ can be written as

$$\frac{\omega_{CK}^2}{\omega_c^2} = \frac{6\eta}{(2 + \cos\theta_0)(1 - \cos\theta_0)}. \tag{3.12}$$

Comparing the (3.11) and (3.12) for $Bo = 0$, it is shown that the present model yields better predictions due to the incorporation of the contribution of the kinetic energy of the internal flow through ζ.

3.3. *Model predictions for finite Bond numbers*

Since numerical solutions are required for the model parameters η, ξ and ζ, the present model, similar to the C–K model, is semi-analytical. Nevertheless, once these parameters are established, as shown in (3.2), (3.3), (3.8), the explicit expression (3.10) is ready to predict the natural frequencies for the lateral oscillation of drops pinned on a vertical surface with different θ_0 and Bo.

The predictions of ω/ω_c by the present, B–S and C–K models are compared with the present experimental results for finite Bo in table 3. The results are also plotted in figure 6. Since the C–K model neglects the effect of kinetic energy of the fluid motion within the drop, it significantly under-predicts the frequency, by up to 21 %. In contrast, the B–S model, which neglects the effect of Bo, over-predicts the frequency, by up to 17 %. As shown in figure 4, the present model yields very similar results to the B–S model for $Bo = 0$ in the range of θ_0 considered in the present experiments. By incorporating the contribution of Bo, the present model yields more accurate predictions than the other two models for all cases. The relative errors are less than 12 % for all cases. Excluding the cases for copper, the errors are less than 9 %.

The present model over-predicts the frequency for all cases, compared with the experimental results. There are a couple of potential reasons that contribute to the discrepancy between the model and experimental results. Similar to the B–S and C–K models, the contact area is taken to be a circle with radius as $R_c = R_0 \sin\theta_0$ in the present model. This ideal contact area corresponds to the spherical-cap shape of the drop when

https://doi.org/10.1017/jfm.2021.844 Published online by Cambridge University Press

Substrate	V_d (μl)	θ_0 (deg.)	Bo	$\left(\frac{\omega}{\omega_c}\right)_{exp}$	$\left(\frac{\omega}{\omega_c}\right)_{mod}$	ε_{mod} (%)	$\left(\frac{\omega}{\omega_c}\right)_{BS}$	ε_{BS} (%)	$\left(\frac{\omega}{\omega_c}\right)_{CK}$	ε_{CK} (%)
Al 6061	3.30	74.60	0.116	2.726	2.878	5.3	2.924	7.3	2.175	−20.2
	3.79	74.50	0.127	2.586	2.773	6.7	2.827	9.3	2.097	−18.9
	4.29	72.15	0.138	2.745	3.013	8.9	3.054	11.3	2.282	−16.9
	4.78	73.60	0.149	2.699	2.926	7.8	2.976	10.2	2.218	−17.8
Cu 110	3.30	85.85	0.116	2.163	2.333	7.3	2.396	10.8	1.760	−18.7
	3.79	84.80	0.127	2.134	2.376	10.2	2.441	14.4	1.794	−15.9
	4.29	87.10	0.138	2.022	2.276	11.2	2.342	15.8	1.720	−14.9
	4.78	84.10	0.149	2.115	2.401	11.9	2.472	16.9	1.817	−14.1
Polystyrene	3.30	91.55	0.116	1.959	2.106	7.0	2.156	10.0	1.586	−19.0
	3.79	92.20	0.127	1.890	2.080	9.1	2.130	12.7	1.568	−17.0
	4.29	93.50	0.138	1.867	2.029	8.0	2.082	11.5	1.531	−18.0
	4.78	91.75	0.149	1.903	2.091	9.0	2.148	12.9	1.580	−16.9
PTFE	3.30	100.10	0.116	1.702	1.812	6.1	1.834	7.8	1.361	−20.2
	3.79	99.85	0.127	1.702	1.817	6.4	1.846	8.5	1.367	−19.7
	4.29	101.20	0.138	1.683	1.772	5.0	1.802	7.0	1.334	−20.7
	4.78	101.05	0.149	1.686	1.773	4.9	1.807	7.2	1.338	−20.6
Wax	3.30	105.10	0.116	1.550	1.660	6.8	1.668	7.6	1.244	−19.7
	3.79	103.95	0.127	1.543	1.691	8.8	1.708	10.7	1.270	−17.7
	4.29	104.65	0.138	1.574	1.667	5.6	1.683	6.9	1.254	−20.3
	4.78	105.30	0.149	1.562	1.644	5.0	1.661	6.3	1.240	−20.6

Table 3. Comparison between experimental results of the normalized frequency ω/ω_c and model predictions with the present, B–S and C–K models.

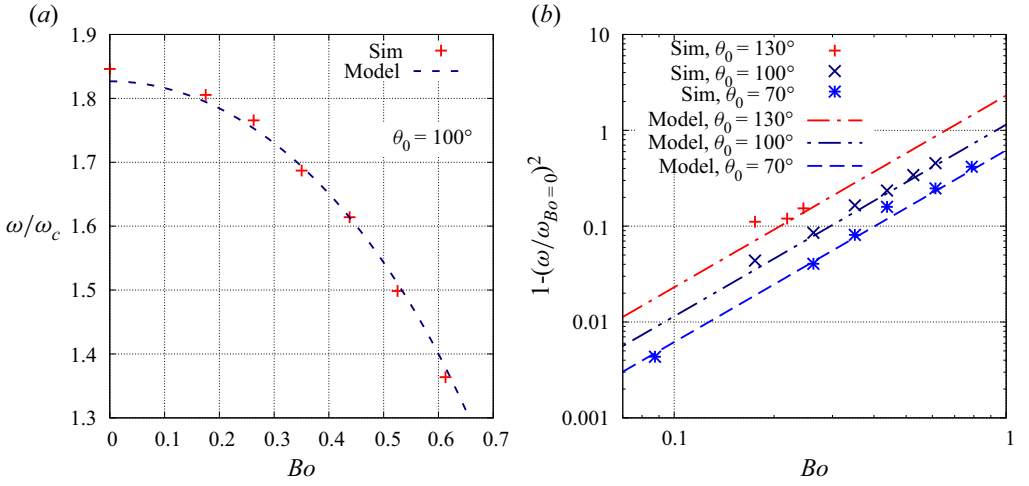

Figure 7. Comparison between the model and simulation results for oscillation frequency as a function of Bo and θ_0.

gravity is absent. The contact area is then fixed during oscillation, since the contact line is pinned. In the experiment, the contact area may be slightly smaller than the ideal contact area considered in the model, since gravity is present when the drop is deposited on the surface. The smaller contact area will result in a weaker constraint on the drop and a lower oscillation frequency. Furthermore, although in the experiment the oscillation amplitude is controlled to be very small, the contact line may still not be fully pinned and may have oscillated with a very small amplitude near the equilibrium position. In contrast, the contact line is perfectly pinned in the model and simulation. The mobility of the contact line will result in a reduction of the oscillation frequency for the same θ_0 and Bo, according to our previous study (Sakakeeny & Ling 2021).

In the experiment, Bo is varied only in a very small range ($0.12 < Bo < 0.15$). Drops with larger Bo are very unstable and may slide even when the surface vibration amplitude is very small. To better pin the contact line and to enable experiments for larger Bo, a more sophisticated surface treatment, such as that by Chang *et al.* (2015), is required, which will be relegated to future work. In order to validate the model for higher Bo, the model predictions are compared with the fully resolved simulation results.

The model and simulation results of the normalized frequency ω/ω_c as a function of Bo for $\theta_0 = 100°$ are shown in figure 7(*a*). It is seen that ω/ω_c decreases with Bo and excellent agreement between the present model and the simulation results is observed. It is conventionally considered that the effect of gravity on the the supported drop oscillation is negligible if $Bo < 1$, namely when the drop radius is smaller than the capillary length (Chang *et al.* 2015). However, it can be seen that the frequency decreases for more than 25 % when Bo increases from 0 to 0.62.

The variation of ω/ω_c over Bo can be better depicted if ω is normalized by its $Bo = 0$ counterpart $\omega_{Bo=0}$. From (3.10), it can be shown that

$$\omega^2/\omega_{Bo=0}^2 = 1 + (3\xi/2\eta^3)Bo_1^2. \tag{3.13}$$

The equilibrium drop results show that $\xi < 0$ for all θ_0 (see figure 5*a*), indicating that that the curvature of the S–y_c curve (3.1) decreases as y_c increases. As a result, ω/ω_c decreases with Bo, see figure 7(*a*). Furthermore, the leading correction term for $\omega^2/\omega_{Bo=0}^2$ scales

with Bo^2. Therefore, for finite and small Bo, ω/ω_c decreases quadratically with Bo. It is difficult to vary Bo over a wide range in experiments to examine the scaling relation, but that can be done in the simulations. We have change g from 0 to 0.9 m s^{-2}, yielding $0 \leq Bo \leq 0.78$. The model and simulation results for $\theta_0 = 70^\circ$, 100° and 130° are plotted in figure 7(*b*). Since drops with large θ_0 become unstable for large Bo, the range of Bo for $\theta_0 = 130^\circ$ is smaller than other cases. The model predictions (3.13) agree very well with the simulation results, validating the quadratic scaling law revealed in the model.

In the present study, Bo is varied by changing the gravity g. Therefore, the results imply that the natural frequency of the lateral oscillation mode will increase if the drops oscillations occur in a reduced gravity environment. This knowledge is important to the surface vibration dropwise condensation applications in the space station.

The present model can also be used to estimate the frequencies for the drops of different volume. For a given gravity, Bo increases with V_d. As a result, ω/ω_c decreases as V_d increases. Since the model is based on an inviscid assumption and the viscous effect on the oscillation frequency (Lamb 1932; Prosperetti 1980) is not accounted, it is valid only for $Oh \ll 1$. For low-viscosity liquids like water, Oh for millimetre drops is generally small. Yet, as Oh increases as the drop size decreases, caution is required if the model is applied to very small drops.

Acknowledgement. The authors also thank Professor S. Zaleski for the helpful discussions on numerical model of pinned contact lines.

Funding. This work was supported by the startup fund at Baylor University and the National Science Foundation (1942324). The Baylor High Performance and Research Computing Services (HPRCS) have provided the computational resources that have contributed to the research results reported.

Declaration of interests. The authors report no conflict of interest.

Author ORCIDs.
J. Sakakeeny https://orcid.org/0000-0002-8368-9127;
Y. Ling https://orcid.org/0000-0002-0601-0272.

References

Afkhami, S., Buongiorno, J., Guion, A., Popinet, S., Saade, Y., Scardovelli, R. & Zaleski, S. 2018 Transition in a numerical model of contact line dynamics and forced dewetting. *J. Comput. Phys.* **374**, 1061–1093.

Afkhami, S. & Bussmann, M. 2009 Height functions for applying contact angles to 3d VOF simulations. *Intl J. Numer. Meth. Fluids* **61** (8), 827–847.

Boreyko, J.B. & Chen, C.-H. 2009*a* Restoring superhydrophobicity of lotus leaves with vibration-induced dewetting. *Phys. Rev. Lett.* **103**, 174502.

Boreyko, J.B. & Chen, C.-H. 2009*b* Self-propelled dropwise condensate on superhydrophobic surfaces. *Phys. Rev. Lett.* **103**, 184501.

Bostwick, J.B. & Steen, P.H. 2014 Dynamics of sessile drops. Part 1. Inviscid theory. *J. Fluid Mech.* **760**, 5–38.

Celestini, F. & Kofman, R. 2006 Vibration of submillimeter-size supported droplets. *Phys. Rev.* E **73**, 041602.

Chang, C.-T., Bostwick, J.B., Daniel, S. & Steen, P.H. 2015 Dynamics of sessile drops. Part 2. Experiment. *J. Fluid Mech.* **768**, 442–467.

Dai, X., Sun, N., Nielsen, S.O., Stogin, B.B., Wang, J., Yang, S. & Wong, T.-S. 2018 Hydrophilic directional slippery rough surfaces for water harvesting. *Sci. Adv.* **4**, eaaq0919.

Lamb, H. 1932 *Hydrodynamics*. Cambridge University Press.

Noblin, X., Buguin, A. & Brochard-Wyart, F. 2004 Vibrated sessile drops: transition between pinned and mobile contact line oscillations. *Eur. Phys. J.* E **14**, 395–404.

Popinet, S. 2009 An accurate adaptive solver for surface-tension-driven interfacial flows. *J. Comput. Phys.* **228** (16), 5838–5866.

PROSPERETTI, A. 1980 Normal-mode analysis for the oscillations of a viscous-liquid drop in an immiscible liquid. *J. Méc.* **19**, 149–182.

SAKAKEENY, J. & LING, Y. 2020 Natural oscillations of a sessile drop on flat surfaces with mobile contact lines. *Phys. Rev. Fluids* **5**, 123604.

SAKAKEENY, J. & LING, Y. 2021 Numerical study of natural oscillations of supported drops with free and pinned contact lines. *Phys. Fluids* **33**, 062109.

SCARDOVELLI, R. & ZALESKI, S. 1999 Direct numerical simulation of free-surface and interfacial flow. *Annu. Rev. Fluid Mech.* **31**, 567–603.

SHARP, J.S., FARMER, D.J. & KELLY, J. 2011 Contact angle dependence of the resonant frequency of sessile water droplets. *Langmuir* **27**, 9367–9371.

SNOEIJER, J.H. & ANDREOTTI, B. 2013 Moving contact lines: scales, regimes, and dynamical transitions. *Annu. Rev. Fluid Mech.* **45**, 269–292.

STRANI, M. & SABETTA, F. 1984 Free vibrations of a drop in partial contact with a solid support. *J. Fluid Mech.* **141**, 233–247.

STRANI, M. & SABETTA, F. 1988 Viscous oscillations of a supported drop in an immiscible fluid. *J. Fluid Mech.* **189**, 397–421.

YAO, C.W., GARVIN, T.P., ALVARADO, J.L., JACOBI, A.M., JONES, B.G. & MARSH, C.P. 2012 Droplet contact angle behavior on a hybrid surface with hydrophobic and hydrophilic properties. *Appl. Phys. Lett.* **101**, 111605.

YAO, C.-W., LAI, C.-L., ALVARADO, J.L., ZHOU, J., AUNG, K.T. & MEJIA, J.E. 2017 Experimental study on effect of surface vibration on micro textured surfaces with hydrophobic and hydrophilic materials. *Appl. Surf. Sci.* **412**, 45–51.